Interferometric Sounding Using a Metamaterial-based Compressive Reflector Antenna

Ali Molaei, Juan Heredia Juesas, William Blackwell, Jose A. Martinez Lorenzo

Abstract—This paper describes a new coded interferometric system for sensing the physical temperature radiated from the Earth's surface. The proposed system consists of a Compressive Reflector Antenna (CRA) coated with Metamaterial Absorbers (MMA). The CRA and the MMA are used to code the received electromagnetic field in space and in frequency, at the focal plane array. The MMA is modeled by an equivalent magneto-dielectric medium having a definite thickness. A high frequency method based on Physical Optics is used to build the sensing matrix of the system, and the inverse problem is solved using a Nesterovbased Compressive Sensing methodology. Numerical examples are carried out in order to reconstruct the physical temperature of the Earth's surface. The performance of the proposed system is compared to that of the conventional interferometric system GeoSTAR. Preliminary results show that the metamaterial-based CRA provides comparable performance to the GeoSTAR configuration with only half of the feeding elements, while keeping the same physical aperture size for the two configurations.

Index Terms—compressive reflector antenna, phased array, metamaterial absorber, radio interferometry, imaging.

I. INTRODUCTION

RADIO interferometry has been widely used for sounding the Earth's atmosphere [1]–[4]. The GeoSTAR system is one of the most successful interferometers [2], [5], and its operation is based on performing complex cross-correlations between the measured field by each pair of receivers in a Y-shaped array. These complex cross-correlated signals, which are characterized by the spatial coherence function of the electromagnetic (EM) field, are used to reconstruct the physical temperature of the Earth's atmosphere. The main drawbacks with these conventional interferometer systems are their physical dimension, overall weight, and the large number of receiving modules and correlators.

The aforementioned drawbacks in current sensing and imaging systems may be overcome by the use of metamaterial absorbers (MMAs) [6]–[11], which were originally introduced by Landy et al. [8]. Specifically, by using an array of MMAs, in which each element of the array presents a near-unity absorption at a specified frequency, one can produce codes that are changed with the instantaneous frequency of the radar chirp, as presented in [12]. As a result, the number of transmitters and receivers required to provide a suitable imaging performance is drastically reduced. Recently, the same outcome was achieved by using a Compressive Reflector Antenna (CRA), which has the ability to provide spatial coding in the focal plane array region [13]–[18].

In this work, the performance of a CRA is further improved by coating its surface with multiple MMAs, so that both spectral and spatial codes can be simultaneously produced, as shown in Fig. 1. As a result, the sensing capacity of

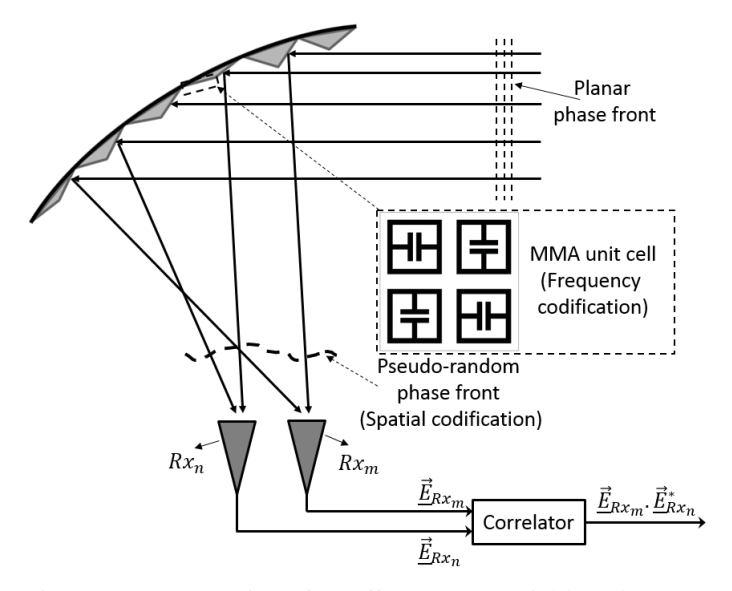


Fig. 1: 2D cross-section of an offset metamaterial-based CRA.

the system is enhanced [17]; this results in a reduction in the number of receiving modules, while keeping the imaging performance similar to that provided by the GeoSTAR interferometric system. The performance of the doubly-curved pseudo-randomly distorted CRA-MMA system requires an accurate characterization of the bulk behavior of the MMAs, which involves modeling the scattering phenomenon at several spatial scales (spanning five orders of magnitude) for arbitrary oblique incident excitations. For this purpose, a semi-analytical model, based on a multi-layer Drude-Lorentz model [7], is also presented in this work. This model is capable of characterizing the electric and magnetic response of the electric-field-coupled absorber (ELCA) metamaterials, which is later used to characterize the reflection coefficient of the multi-layer MMA. These coefficients are coupled into a high frequency method, the Modified Equivalent Current Approximation (MECA) [19], in order to assess the performance of the imaging system.

The presented CRA relies on the use of norm-1 regularized iterative Compressive Sensing (CS) imaging techniques, and a few relevant ones are discussed next. (a) Bayesian CS [20]–[24] enforces a probabilistic hierarchical prior as a sparsity regularization constraint. It has been shown in [24] that by employing the formerly studied relevance vector machine from the sparse Bayesian learning literature, problems in CS can be solved more effectively and faster compared to the state-of-the-art algorithms. (b) FISTA [25] is an extension of the classical gradient algorithm. It preserves the computational simplicity of ISTA, but it possesses a global rate of convergence that is significantly faster than the latter. (c) ADMM, [26], [27] is a

consensus-based imaging algorithm. It is a simple but effective algorithm that is appropriate to solve in a distributed fashion large convex optimization problems. (d) NESTA [28] is a robust first-order method that solves basis-pursuit problems. The techniques used in the NESTA algorithm —provided as a MATLAB toolbox [29]— are based on the solution proposed by Nesterov [30] to smooth non-convex problems, combined with an improved first-order method [31] that was proven to have an enhanced convergence rate. In this paper, the NESTA toolbox [29] is adopted for solving the inverse problem, as it is suitable for solving large scale CS problems due to its fast convergence rate; however, other CS solvers could have been used as well.

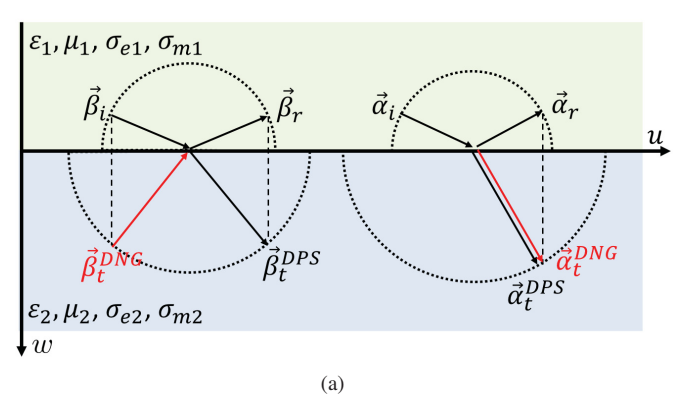
The rest of the paper is organized as follows: Section II introduces the semi-analytical model used for characterizing the oblique incidence reflection coefficient of the ELCA. Section III describes the structure of the CRA, the mathematical analysis of the cross-correlation radiometry, the computation of the sensing matrix for imaging, and the use of CS techniques for performing the imaging. Section IV presents the following results: 1) optimization of the semi-analytical model of the ELCA; and 2) imaging using the proposed CRA-MMA. Section V provides a final summary and conclusions.

II. SEMI-ANALYTICAL MODEL FOR CHARACTERIZING THE ELCA OBLIQUE INCIDENCE REFLECTION COEFFICIENT

A semi-analytical model is presented to characterize the EM response of the ELCA metamaterials. The semi-analytical model is derived in three steps: 1) the reflection coefficient for the multi-layered magneto-dielectric media, characterized by using the Drude-Lorentz parameters of each medium, is analytically derived; 2) simulations based on HFSS Finite Elements Method (FEM) are used to compute the reflection coefficient of the ELCA; and 3) the Drude-Lorentz parameters of a three-layered media are optimized in order to find the bulk parameters that best fit the FEM-simulated ELCA. The semianalytical model is capable of accounting for the characteristic resonances of the ELCA metamaterial; and it is valid for both TE and TM polarizations and for a wide range of incident field angles. For the sake of generality, the next two subsections derive the parameters used for modeling the wavepropagation in a two-layers and a three-layers lossy isotropic media; these parameters will be optimized afterwards in order to characterize the scattering of the proposed CRA-MMA imaging system.

A. Generalized Wave-Propagation Law for Lossy Isotropic Media

A wave propagating in a lossy and isotropic medium is characterized by the complex wave vector $k = \beta - i\alpha$, where eta and lpha are real-valued propagation and attenuation vectors, respectively [32]. In the general case, this wave is obliquely incident into another lossy and isotropic medium, as shown in Fig. 2(a). The propagation and attenuation vectors in each medium point in different directions. Each medium is characterized by their complex permittivity and permeability $[\varepsilon_i, \mu_i, \sigma_{ei}, \sigma_{mi}]$, where ε_i is the real part of



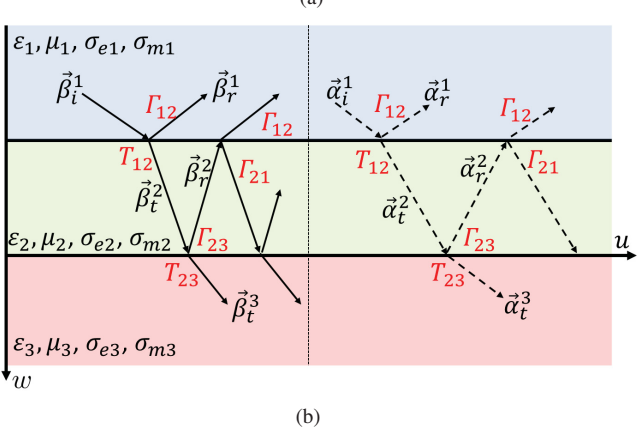


Fig. 2: (a) Phase and attenuation wave vector for a plane wave obliquely incident on a half-space inhomogeneous medium. Second medium could be DNG (red line) or DPS (black line). (b) Schematic of the generalized three-layer stratified model.

permittivity, μ_i is the real part of permeability, σ_{ei} is the electric conductivity, and σ_{mi} is the magnetic conductivity for the i-th medium. According to the phase-matching condition, the tangential components -u components in Fig. 2(b)- of the second medium's wave vector must be equal to the tangential components of the incident field wave vector. As a result, the transverse components of the wave-vector in the second medium can be computed using the following dispersion relationship:

$$\mathbf{k}^t \cdot \mathbf{k}^t = \omega^2 (\mu_2 - j \frac{\sigma_{m_2}}{\omega}) (\varepsilon_2 - j \frac{\sigma_{e_2}}{\omega})$$
 (1a)

$$\mathbf{k}^{t} \cdot \mathbf{k}^{t} = \omega^{2} (\mu_{2} - j \frac{\sigma_{m_{2}}}{\omega}) (\varepsilon_{2} - j \frac{\sigma_{e_{2}}}{\omega})$$
(1a)
$$\mathbf{k}^{r} \cdot \mathbf{k}^{r} = \omega^{2} (\mu_{1} - j \frac{\sigma_{m_{1}}}{\omega}) (\varepsilon_{1} - j \frac{\sigma_{e_{1}}}{\omega})$$
(1b)

in which: $k^i = \beta^i - j\alpha^i$, $k^r = \beta^r - j\alpha^r$ and $k^t = \beta^t - j\alpha^r$ $j\alpha^t$ are the incident, reflected and transmitted wave vectors, respectively. Equations (1a) and (1b) can be rewritten in terms of the real and imaginary parts of the reflected and transmitted wave vectors as follows:

$$\left|\boldsymbol{\beta}^{t}\right|^{2} - \left|\boldsymbol{\alpha}^{t}\right|^{2} = \omega^{2} \mu_{2} \varepsilon_{2} - \sigma_{e_{2}} \sigma_{m_{2}} \tag{2a}$$

$$|\boldsymbol{\beta}^{\boldsymbol{r}}|^2 - |\boldsymbol{\alpha}^{\boldsymbol{r}}|^2 = \omega^2 \mu_1 \varepsilon_1 - \sigma_{e_1} \sigma_{m_1}$$
 (2b)

$$2\boldsymbol{\alpha}^t \cdot \boldsymbol{\beta}^t = \omega(\varepsilon_2 \sigma_{m_2} + \mu_2 \sigma_{e_2}) \tag{2c}$$

$$2\boldsymbol{\alpha}^{r} \cdot \boldsymbol{\beta}^{r} = \omega(\varepsilon_{1}\sigma_{m_{1}} + \mu_{1}\sigma_{e_{1}}) \tag{2d}$$

The transverse components $(\beta_w^t, \beta_w^r, \alpha_w^t)$ and α_w^r of β and

 α can now be computed in terms of β_u^i and α_u^i as follows:

$$\beta_w^t = \pm \sqrt{\frac{A_2 + \sqrt{A_2^2 + 4B_2^2}}{2}}; (3a)$$

$$\beta_w^r = \pm \sqrt{\frac{A_1 + \sqrt{A_1^2 + 4B_1^2}}{2}} \tag{3b}$$

$$\alpha_w^t = \sqrt{\frac{-A_2 + \sqrt{A_2^2 + 4B_2^2}}{2}};$$
 (3c)

$$\alpha_w^r = -\sqrt{\frac{-A_1 + \sqrt{A_1^2 + 4B_1^2}}{2}} \tag{3d}$$

where

$$A_1 = \omega^2 \mu_1 \varepsilon_1 - \sigma_{e_1} \sigma_{m_1} - (\beta_u^{i^2} - \alpha_u^{i^2})$$
 (4a)

$$A_{2} = \omega^{2} \mu_{2} \varepsilon_{2} - \sigma_{e_{2}} \sigma_{m_{2}} - (\beta_{u}^{i^{2}} - \alpha_{u}^{i^{2}})$$
 (4b)

$$B_1 = \frac{1}{2}\omega(\varepsilon_1\sigma_{m1} + \mu_1\sigma_{e_1}) - \alpha_u^i \beta_u^i$$
 (4c)

$$B_2 = \frac{1}{2}\omega(\varepsilon_2\sigma_{m2} + \mu_2\sigma_{e_2}) - \alpha_u^i\beta_u^i$$
 (4d)

The signs for β_w^t and β_w^r in equations (3a) and (3b) are selected by the material behavior, whether double positive (DPS) or double negative (DNG), according to Table I. The correct directions for the wave vectors are shown in Fig. 2(a).

TABLE I: Signs for the propagation and attenuation numbers in DPS and DNG media.

MEDIUM \COMPONENT	β_w^t	β_w^r	α_w^t	α_w^r
DPS	+	_	+	_
DNG	_	+	+	_

B. Reflection from a Three-Layer Magneto-dielectric Medium

The MMA array can be characterized by solving a three-layer magneto-dielectric medium problem, where an incident field is obliquely impinging on a magneto-dielectric medium, of thickness d, which is backed by a metallic layer. The magneto-dielectric and metallic layers may be characterized by the Drude-Lorentz model [7]:

$$\tilde{\varepsilon}_r(\omega) = \varepsilon_{\inf} + \frac{\omega_{p,e}^2}{\omega_{0,e}^2 - \omega^2 - j\gamma_e\omega}$$
 (5a)

$$\tilde{\mu}_r(\omega) = \mu_{\inf} + \frac{\omega_{p,m}^2}{\omega_{0,m}^2 - \omega^2 - j\gamma_m\omega}$$
 (5b)

in which, ε_{\inf} and μ_{\inf} are the static permittivity and permeability at infinite frequency, $\omega_{p,e}$ and $\omega_{p,m}$ are plasma frequencies, $\omega_{0,e}$ and $\omega_{0,m}$ are resonant frequencies, and γ_e and γ_m are damping frequencies.

A derivation of the total reflection coefficient Γ from a stratified three-layer medium, for any oblique incidence, is presented in Appendix A; and the simplified equation for Γ is derived to be as follows:

$$\Gamma = \Gamma_{12} + \frac{T_{12}\Gamma_{23}T_{21}e^{-j2\Phi^{trans}}}{1 - \Gamma_{23}\Gamma_{21}e^{-2j\Phi^{trans}}}$$

$$= \frac{\Gamma_{12} - \Gamma_{12}\Gamma_{23}\Gamma_{21}e^{-j2\Phi^{trans}} + T_{12}\Gamma_{23}T_{21}e^{-j2\Phi^{trans}}}{1 - \Gamma_{23}\Gamma_{21}e^{-2j\Phi^{trans}}}$$
(6)

In equation (6), Γ_{ij} and T_{ij} are, respectively, the reflection and transmission coefficients associated with the interface between medium i and medium j. The term $e^{-j\Phi^{trans}}$ accounts for the phase delay and amplitude attenuation associated with the wave traveling from the first interface into the second one, or vice versa.

III. METAMATERIAL-BASED COMPRESSIVE REFLECTOR ANTENNA FOR INTERFEROMETRIC RADIOMETRY

A. Compressive Reflector Antenna structure

High-capacity imaging systems using a CRA are characterized by their ability to create spatial coding of the electromagnetic field in the imaging domain [13]–[16]. A CRA can be obtained by placing random Perfect Electric Conductor (PEC) scatterers on the surface of a conventional parabolic reflector. Such a CRA produces pseudo-random spatial patterns in both its focal plane and far-field regions. Moreover, the frequency-dependent response of MMAs enables the CRA to create spatially-dependent spectral codes. As a result, each element in the array used in conjunction with the CRA will possess a unique near- and far- field pattern acting as a spectral and spatial code. This coding mechanism is similar to that described in [33]. Figure 1 shows the 2D cross-section of the proposed CRA-MMA.

B. Mathematical development for cross-correlation interferometric radiometry

The relationship between the data collected and the brightness temperature distribution of the Earth's surface is obtained as follows: for each frequency, the field measured by one receiver is cross-correlated with those of the remaining receivers, as shown in Fig. 3 [34]. The auto- and cross- correlation are described, respectively, by the following equations:

$$\mathbf{E}_{m}^{l}(f) \cdot \mathbf{E}_{m}^{l*}(f) \doteq Ak_{B}B_{m}G_{m}(T_{Am} + T_{RECm}) \tag{7a}$$

$$\mathbf{E}_{m}^{l}(f) \cdot \mathbf{E}_{n}^{l*}(f) \doteq Ak_{B}\sqrt{B_{m}B_{n}}\sqrt{G_{m}G_{n}}V_{mn}^{l}(u_{mn}^{l}, v_{mn}^{l}) \tag{7b}$$

in which $\mathbf{E}_i^l(f)$, for $i \in \{m,n\}$, is the analytical signal collected by the channel i at the center frequency f_l ; the symbol * denotes the complex conjugate; k_B is the Boltzmann constant; T_{Ai} is the antenna's temperature; B_i is the equivalent noise bandwidth; G_i is the power gain of the channel; and A is a constant. The visibility function, which can be expressed

$$\begin{split} V^l_{mn}(u^l_{mn},v^l_{mn}) &= \frac{1}{k_B\sqrt{B_mB_n}\sqrt{G_mG_n}} \mathbf{E}^l_m(f) \cdot \mathbf{E}^{l*}_n(f), \\ \text{is defined in the spatial frequency domain } (u^l_{mn},v^l_{mn}) &\doteq (x_n-x_m,y_n-y_m)/\lambda_l, \text{ where } \lambda_l = c/f_l, \text{ with } c \text{ being the} \end{split}$$

speed of light in free space. From the Van-Cittert Zernicke theorem [35], the visibility function is related to the brightness temperature distribution as follows:

$$V_{mn}^{l} = \frac{1}{\sqrt{\Omega_{m}\Omega_{n}}} \iint_{\xi^{2}+\eta^{2} \leq 1} \frac{T_{B}(\xi,\eta) - T_{REC}}{\sqrt{1-\xi^{2}-\eta^{2}}} \times F_{m}(\xi,\eta) F_{n}^{*}(\xi,\eta) \tilde{r}_{mn}^{l} \left(-\frac{u_{mn}^{l}\xi + v_{mn}^{l}\eta}{f_{l}}\right) \times e^{-j2\pi(u_{mn}^{l}\xi + v_{mn}^{l}\eta)} d\xi d\eta$$

$$(9)$$

where Ω_i is the equivalent solid angle of the antennas;

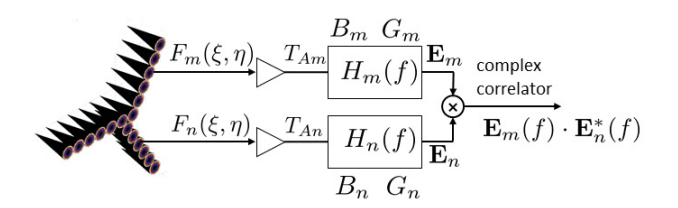


Fig. 3: Interferometric radiometry scheme. The EM field measured by each pair of receivers is cross-correlated. The scheme represents all the parameters involved in the process.

 $\frac{1}{\sqrt{1-\xi^2-\nu^2}}$ is the obliquity factor, $F_i(\xi,\eta)$ is the normalized antenna pattern, $(\xi,\eta)=(sin\theta cos\phi,sin\theta sin\phi)$ are the directional cosines, $T_B(\xi,\eta)$ is the brightness temperature of the scene, T_{REC} is the physical temperature of the receiver (the so-called Corbella's term [36]), and $\tilde{r}^l_{mn}(-\frac{u^l_{mn}\xi+v^l_{mn}\eta}{f_l})$ is the so-called fringe-washing function that can be expressed as

$$\tilde{r}_{mn}^{l} = \frac{e^{-j2\pi f_{0}t}}{\sqrt{B_{m}B_{n}}} \int_{f_{l} - \frac{\Delta f}{2}}^{f_{l} + \frac{\Delta f}{2}} H_{m}(f) H_{n}^{*}(f) e^{j2\pi f t} df, \quad (10)$$

where $H_i(f)$ is the frequency response and Δf is the bandwidth of channel f_l .

Equation (9) can be simplified under certain conditions, [34]. For a narrow bandwidth and reduced dimensions of the array, the fringe-washing function becomes $\tilde{r}_{mn}^l \approx 1$. Furthermore, assuming that the patterns of the horn antennas are identical, that is $F_m = F_n$, and neglecting the temperature of the receiver, the visibility function and the brightness temperature are now related as follows:

$$V_{mn}^{l} = \iint_{\xi^{2} + \eta^{2} \le 1} T(\xi, \eta) e^{-j2\pi (u_{mn}^{l} \xi + v_{mn}^{l} \eta)} d\xi d\eta \qquad (11)$$

where

$$T(\xi, \eta) = \frac{T_B(\xi, \eta)}{\sqrt{1 - \xi^2 - \eta^2}} |F_n(\xi, \eta)|^2$$
 (12)

is the modified brightness temperature for each direction (ξ,η) . Under these conditions, the mentioned modified brightness temperature can be recovered by the inverse 2D Fourier transform of the visibility function, $T(\xi,\eta) = \mathcal{F}^{-1}[V^l_{mn}(u^l_{mn},v^l_{mn})].$

In the case of the CRA, some of the previous simplifications are not valid. Specifically, the phase front produced on the receiving array by a source whose radiation is coming from

a given direction (ξ_0,η_0) is not planar anymore. This is due to the spectral and spatial coding produced by the CRA when an incoming wave is reflected towards the receiving array–see Fig. 1. This coding also makes the far-field patterns produced by each horn antenna, after interacting with the CRA, to be different from one another, that is $F_m \neq F_n$. Taking this into consideration, the modified brightness temperature from equation (9) is now given by

$$T(\xi, \eta) = \frac{T_B(\xi, \eta)}{\sqrt{1 - \xi^2 - \eta^2}} \tilde{F}_n(\xi, \eta) \tilde{F}_m^*(\xi, \eta),$$
 (13)

where

$$\tilde{F}_{i}(\xi, \eta) = \max_{f \in [f_{1} - \frac{\Delta f}{2}, f_{N_{f}} + \frac{\Delta f}{2}]} \{F_{i}(\xi, \eta, f_{l})\}$$
(14)

as shown in Fig. 4. N_f is the total number of frequencies.

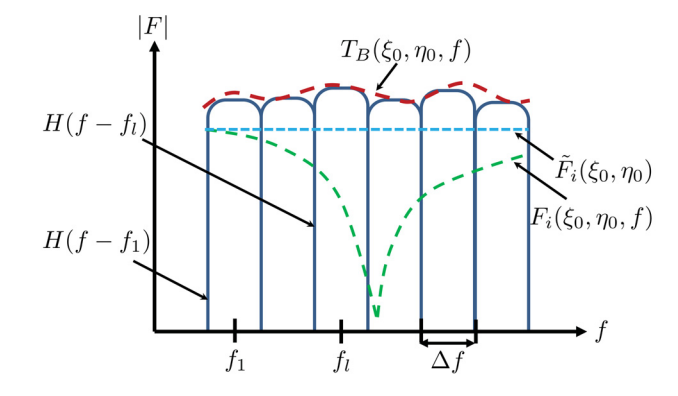


Fig. 4: Frequency modulation of the antenna pattern due to the MMAs.

Then, the appropriate equation that relates the temperature to the visibility function takes the following form:

$$V_{mn}^{l} = \iint_{\xi^{2} + \eta^{2} \le 1} T(\xi, \eta) C_{m}^{l}(\xi, \eta) C_{n}^{l*}(\xi, \eta) \times e^{-j\phi_{m}(\xi, \eta)} e^{j\phi_{n}(\xi, \eta)} d\xi d\eta$$

$$(15)$$

where

$$C_i^l(\xi,\eta) = \frac{F_i(\xi,\eta,f_l)}{\tilde{F}(\xi,\eta)},\tag{16}$$

for $i \in \{m,n\}$, is the code produced by the CRA coated with the MMA at the aperture of the horn antenna i at the center frequency f_l . It is important to remark that, by the use of the CRA, the phase difference between each pair of antennas is not linear anymore $\phi_m^l(\xi,\eta) - \phi_n^l(\xi,\eta) \neq 2\pi(u_{mn}^l\xi + v_{mn}^l\eta)$. This reduces the redundancy of the system and the mutual information between each pair of antennas, resulting in an enhanced sensing capacity. This "physical" compression helps to reduce the total number of horn antennas and, consequently, the complexity of the system. In addition, the physical dimensions, weight, budget, and computational costs are reduced, while having a similar performance in terms of imaging quality, when compared to the GeoSTAR configuration.

C. Sensing matrix for Imaging

The reconstructed image is performed in N_p pixels. The interferometric system uses $N_s = N_r \cdot N_r \cdot N_f$ measurements to perform the imaging, where N_r is the number of receivers. The field measured by each receiver is complex cross-correlated with that of the remaining elements of the array. Under this configuration, Eq. (15) can be discretized in order to get a linear matrix equation that relates the visibility $\mathbf{g} \in \mathbb{C}^{N_s}$ (obtained from the measurements) and the unknown brightness distribution for each pixel $\mathbf{r} \in \mathbb{C}^{N_p}$, through a sensing matrix $\mathbf{H} \in \mathbb{C}^{N_s \times N_p}$. This linear relationship can be expressed in a matrix form as follows:

$$\mathbf{g} = \mathbf{H} \cdot \mathbf{r} + \mathbf{w} \tag{17}$$

where $\mathbf{w} \in \mathbb{C}^{N_s}$ represents the noise collected by the correlators from the receiving antennas, for a given frequency.

Each element of the vector \mathbf{g} is defined as $g_q = c_{m,n}^{(1)} \mathbf{E}_m^l \cdot \mathbf{E}_n^{l,*}$, indicating the correlation between the scattered EM fields corresponding to the m-th and n-th measurements, depending on the antenna position and frequency f_l , with $q=1,\ldots,N_s$. The constant $c_{m,n}^{(1)}=1/k_B\sqrt{B_mB_n}\sqrt{G_mG_n}$ relates the correlation of the EM fields with the visibility function, as in Eq. (8).

Each element of the sensing matrix \mathbf{H} is defined as $h_{q,p} = c_{m,n}^{(2)} \mathbf{E}_{m,p}^l \cdot \mathbf{E}_{n,p}^{l,*}$, indicating the correlation between the scattered EM field received by the m-th and n-th elements of the array, for frequency f_l , when they are illuminated by a current source in the p-th pixel of the imaging domain, with $q=1,\ldots,N_s$ and $p=1,\ldots,N_p$. The constant $c_{m,n}^{(2)} = \tilde{F}_n \tilde{F}_m^* / \sqrt{1-\xi^2-\eta^2}$, as in Eq. (13).

The complete expressions of the vector \mathbf{g} and the matrix \mathbf{H} can be found in [14].

D. Compressive Sensing Imaging

The methodology employed for performing the imaging process is carried out through Compressive Sensing (CS) techniques. CS theory was first introduced in [37]. Since then, many other authors contributed to improve that theory—see, for example, [38] and references therein for a review of CS.

The main idea of CS is based on the fact that sparse signals can be recovered from a much smaller number of measurements than those required by the Nyquist sampling criterion. In order to be able to apply CS, the sensing matrix \mathbf{H} has to satisfy the Restricted-Isometry-Property (RIP) condition, which is related to the independence of its columns. In addition, the number of non-zero elements N_{nz} of the reconstructed image \mathbf{r} has to be much smaller than the total number of elements in the image N_p ($N_{nz} \ll N_p$). Assuming both conditions are satisfied, the reconstruction of the unknown vector for the imaging can be performed with a few number of measurements. This reduces the imaging computational cost.

The following convex optimization problem is solved in order to obtain the unknown vector **r**:

$$\min \|\mathbf{r}\|_1 \qquad \text{s.t.} \quad \|\mathbf{H}\mathbf{r} - \mathbf{g}\|_2 < \delta_H \tag{18}$$

where δ_H is an upper bound for the residual error $\|\mathbf{Hr} - \mathbf{g}\|_2$. Many different algorithms have been developed in order to

solve (18), [38], [39]. In this paper, the NESTA algorithm [28], has been used for solving the optimization problem.

IV. NUMERICAL RESULTS

Using the mechanism explained in section II, three MMAs (MMA1, MMA2 and MMA3) were designed to resonate at different frequencies (50 GHz, 52 GHz and 54 GHz). These three MMA designs were randomly used to coat the surface of the CRA. The polarization-independent ELCA was designed using the commercially available software HFSS. Next, the Drude-Lorentz parameters of the three-layer magneto-dielectric medium were optimized in order to match the reflection coefficient of the model and the one obtained from HFSS for a given incident angle. The pattern search method embedded in the MATLAB optimization toolbox was used in order to match these reflection coefficients.

A. MMA Optimization Results

Figure 5 shows the geometry and dimensions of the polarization-independent ELCA metamaterial. The MMA resonating at 52 GHz (MMA2) is designed according to the following parameters: $a=880\mu m,\ l=361\mu m,\ w=63\mu m,\ g=46\mu m,\ d=689\mu m,\ Rogers$ substrate (RO 4835) with permittivity of 3.66, dielectric loss-tangent of 0.0037, and thickness of $110\mu m$. The parameters of the Drude-

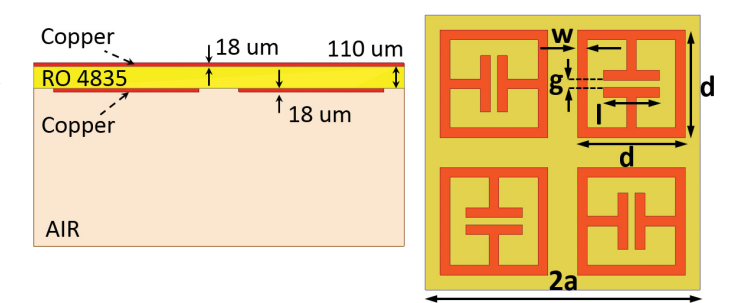


Fig. 5: Schematic of the parameters of the polarization-independent ELCA: (left) cross section view and (right) top view.

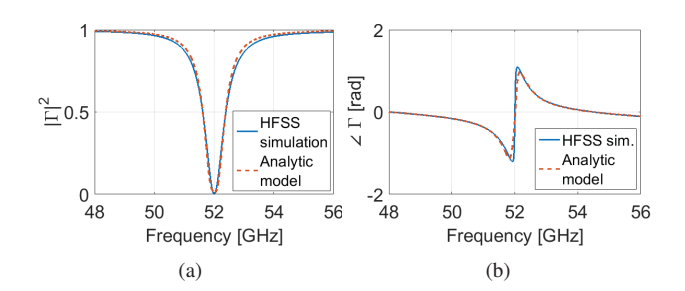


Fig. 6: HFSS and semi-analytical calculation of the total reflection coefficient of the polarization-independent ELCA, when it is excited with a TM-mode and incident angle of 30°: (a) magnitude and (b) phase of the reflection coefficient.

Lorentz model for the middle magneto-dielectric medium are optimized for a TM-wave obliquely impinging the ELCA at an angle of 30° with respect to the normal of the ELCA plane. Figure 6 compares the phase and magnitude-squared of the reflection coefficient obtained with the HFSS software and the semi-analytical model. The optimized Drude-Lorentz parameters are listed in Table II. Then, the performance of the optimized model is evaluated for other incident angles and polarization vectors not used during the optimization step. Figure 7 shows the phase and magnitude squared of the reflection coefficient of TEM-mode, TE-mode for 45°, and TM-mode for 45° incident angles. The results show that the semi-analytical model is capable of accurately matching the resonance behavior of the ELCA metamaterial for TEM, TE, and TM modes at different incident angles. MMA1 and MMA3 are designed following the same method. Figure 8(a) illustrates the magnitude squared of reflection coefficient versus frequency for the MMAs. Figures 8(b), 8(c), and 8(d) represent the PEC scatterer facets associated randomly with MMA1, MMA2, and MMA3, respectively.

TABLE II: Drude-Lorentz parameters for the magneto-dielectric media.

PAR.	VALUE	PAR.	VALUE
ε_{inf}	2.9	μ_{inf}	3.1
$\omega_{p,e}$	$2\pi \times 9.01~GHz$	$\omega_{p,m}$	$2\pi \times 7.55 \ GHz$
$\omega_{0,e}$	$2\pi \times 52~GHz$	$\omega_{0,m}$	$2\pi \times 52~GHz$
γ_e	$2\pi \times 341~MHz$	γ_m	$2\pi \times 291~MHz$

B. Interferometric Sounding Results

The performance of the designed metamaterial-based CRA interferometric system is evaluated in a microwave sounding imaging application, and it is then compared with a conventional interferometric system (GeoSTAR). To solve the inverse problem, a traditional pseudo-inverse method and a current state-of-the-art compressive sensing algorithm (NESTA) [28] have been used.

The design parameters used for the numerical simulation are shown in Table III. Nine receiving horns placed in a Yshaped configuration on the focal plane feed the metamaterialbased CRA. Figure 9 shows the geometry of the metamaterialbased CRA and GeoSTAR systems. The original image (Fig. 13(a)) is an example of the physical temperature radiated from the surface of the Earth. The system is assumed to measure EM fields from a geostationary satellite orbiting around the Earth. In Fig. 14, white circles are representing the half-power beamwidth of the antennas covering the surface of the Earth when they are exciting the TRA. Figure 10 shows the radiation pattern of the antennas in the CRA configuration calculated in the imaging domain at 52 GHz. As a result of the spatial coding, each antenna element used in conjunction with the CRA possesses a unique radiation pattern, whose field of view covers the whole imaging domain. Moreover, the Singular Value (SV) distribution of the CRA system is calculated and compared to that of the GeoSTAR system, when nine receiving antennas are used. Figure 11 shows that the SV distribution of the CRA is better than that of the GeoSTAR, which ultimately provides a higher sensing capacity (see Fig. 12) and provides a better reconstruction performance. The sensing capacity of

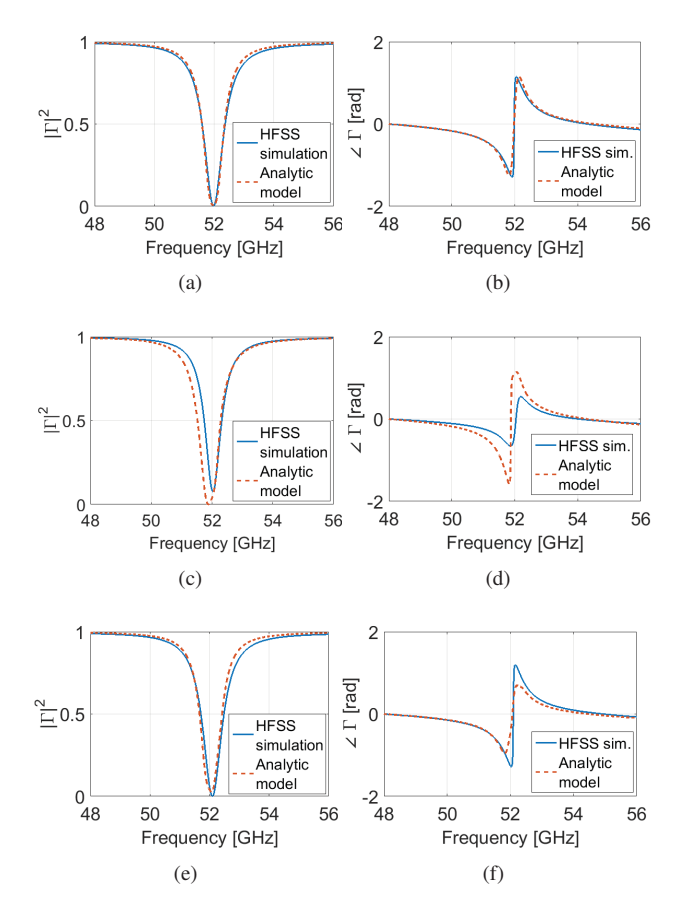


Fig. 7: HFSS and semi-analytical calculation of the total reflection coefficient of the polarization-independent ELCA, when it is excited with a (a), (b) TEM-mode; (c), (d) TE-mode and incident angle of 45° ; and (e), (f) TM-mode and incident angle of 45° .

the imaging systems are calculated according to the following equation:

$$C_{\epsilon}^{M} \approx \log_{2} \left(\prod_{m=1}^{M} \frac{\sigma_{m}^{\mathbf{H}} \cdot e_{m}}{\epsilon} \right) = \sum_{m=1}^{M} \log_{2} \left(\frac{\sigma_{m}^{\mathbf{H}} \cdot e_{m}}{\epsilon} \right) [bits]$$

where $\sigma_m^{\mathbf{H}}$ is the m-th Singular Value (SV) of the sensing matrix \mathbf{H} , e_m is power of the signal received in the m-th orthogonal channel of \mathbf{H} , and M is the number of SVs that are above the uncertainty level ϵ . Figure 12 compares the improved sensing capacity of the CRA as a function of Signal to Noise Ratio (SNR), with that of the GeoSTAR configuration.

The measurements are done in the frequency range of 50-54 GHz. To ensure a fair comparison between the proposed system and GeoSTAR, frequency range and the largest dimension of the aperture for both configurations are set to be equal. However, the metamaterial-based CRA uses half of the horns used by the GeoSTAR configuration, resulting in less data required for the reconstruction.

Figure 13 shows the original and reconstructed images for the metamaterial-based CRA and contrasts it with reconstructed images for the GeoSTAR configuration. No noise has been considered in the image reconstructions presented in this

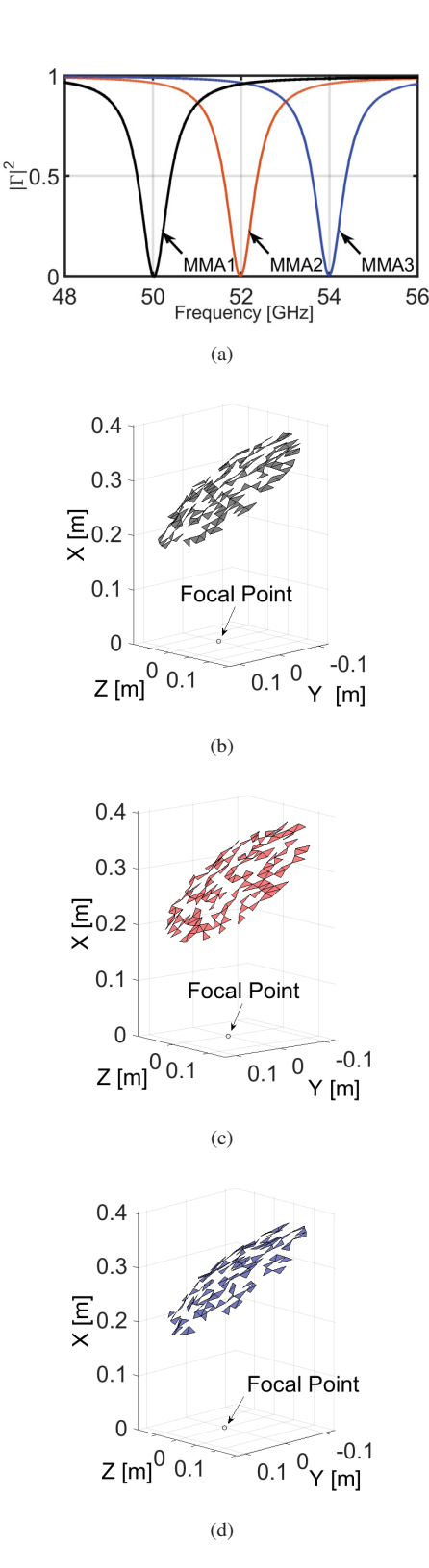


Fig. 8: (a) Magnitude of the reflection coefficient, and PEC scatterer facets associated to (b) *MMA1*, (c) *MMA2* and (d) *MMA3*.

example. In order to calculate the error, the Frobenius norm of the difference between the original and the reconstructed images is computed, and it is normalized by the Frobenius norm of the original image. The reconstructed physical temperature using the pseudo-inverse method for the metamaterialbased CRA and GeoSTAR configuration produces an error of 16.7% and 8.6%, respectively. The error value of the NESTA algorithm for the metamaterial-based CRA and GeoSTAR configuration is 6.9% and 5.5%, respectively. This shows that with the metamaterial-based CRA the number of receivers is substantially reduced in comparison to that of the GeoSTAR system (from eighteen to nine), while keeping similar imaging performance. A comparison between two state of the art CS solvers has also been performed in terms of the reconstruction error. Specifically, NESTA and ADMM solvers have been used for this purpose. The latter presents a 5.8% more error value than the former, showing that NESTA is a suitable choice for this particular problem. An analysis showing the dependence between the image error and the number of receiving antennas has also been performed. In Fig. 15, the image reconstruction error for both the GeoSTAR and CRA configurations is presented when 6, 9, 12, 15, and 18 receiving antennas are used. In all cases, the CRA possesses a lower image error when compared to that of the GeoSTAR configuration, except for the case of six receivers. However, the error for both configurations is unacceptable (larger than 20%)in the latter case, thus making such configuration unreliable for imaging purposes. This study also indicates the minimum number receiving antennas needed to achieve a reconstruction error below a specific value. For example, if an error value below 5% is desired, then twelve receiving antennas are required for the CRA configuration. Note that this error cannot be achieved in the GeoSTAR configuration, even when 18 elements are

A quantitative evaluation of the noise for different signal-to-noise ratios (SNRs) has been carried out for the metamaterial-based CRA configuration. The evaluation shows that a high SNR value is needed in order to have a good image reconstruction. However, by averaging N_s samples in the measurement vector ${\bf g}$, the effect of the noise can be mitigated in terms of the image quality. Figure 16 shows the reconstruction error for different SNR values ranging from 10 dB to 50 dB and for 3 different N_s values. Moreover, reconstructed images for SNR=50 and different N_s values has been presented in Fig. 17. The results demonstrate that by increasing the value of N_s , the reconstruction error converges to that of the noise-less system.

TABLE III: Parameters for the numerical design.

PARAMETERS	CRA	GeoSTAR [2]
Frequency band	50 - 54 GHz	50 - 54 GHz
No. of freq. (N_f)	7	7
Longest Aperture size (D)	25 [cm]	25 [cm]
Diameter of feed elements	2.1 [cm]	2.1 [cm]
No. of feeds (N_r)	9	18
Focal length (f)	14 [cm]	-
Offset height (h_o)	28 [cm]	-

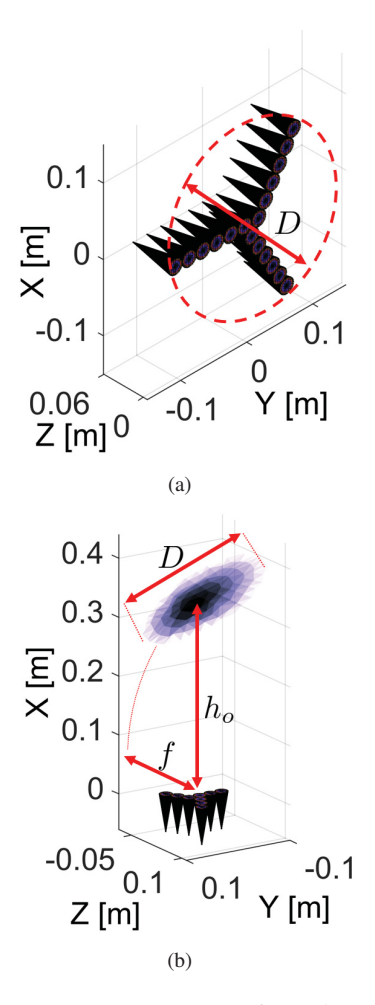


Fig. 9: Geometry: (a) GeoSTAR configuration, (b) Compressive Reflector Antenna.

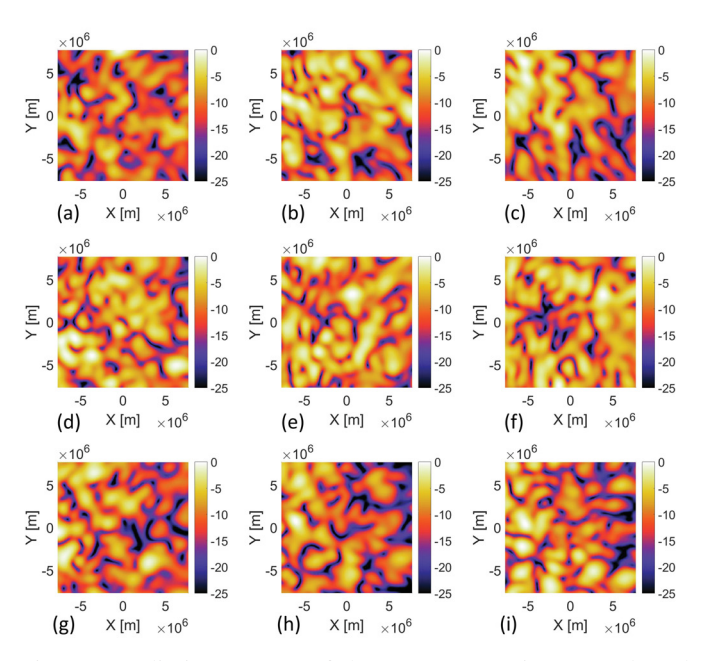


Fig. 10: Radiation pattern of the antennas at 52 GHz, plotted in the reconstruction domain: (a) Ant. 1; (b) Ant. 2; (c) Ant. 3; (d) Ant. 4; (e) Ant. 5; (f) Ant. 6; (g) Ant. 7; (h) Ant. 8; (i) Ant. 9.

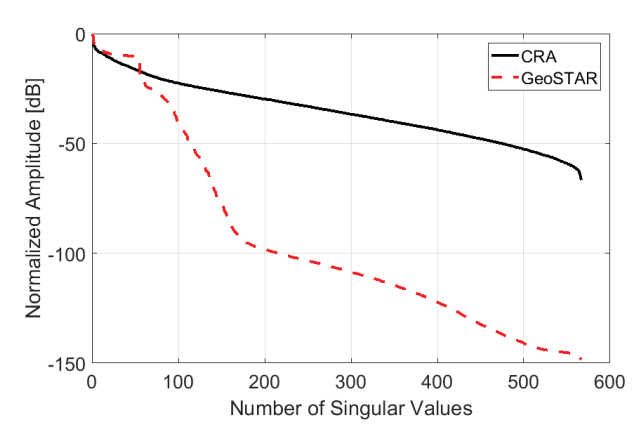


Fig. 11: Comparison of the normalized SV distribution of the CRA and GeoSTAR configurations. Both configurations are considered having 9 antenna elements.

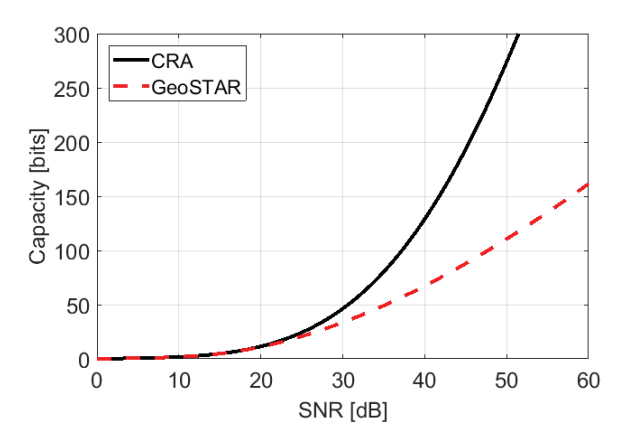


Fig. 12: Comparison of the sensing capacity of the CRA and GeoSTAR configurations. Both configurations are considered having 9 antenna elements.

V. CONCLUSION

This paper presents a novel complex interferometric microwave sounding system, which uses a metamaterial-based CRA. The proposed system generates spatial and spectral coding of the EM field in the imaging domain. A semianalytical model was used to characterize the electromagnetic scattering of the MMAs for a wide range of incident angles. The proposed system substantially reduces the number of receiving elements, while keeping a similar imaging quality. This is due to the fact that the spatial and spectral codes reduce the mutual information between the successive measurements, thus leading to an enhanced sensing capacity of the system. In this work, each MMA has a single resonance as a mechanism to create the spectral coding. Nevertheless, additional research will be performed in order to explore the use of multiple resonances in each MMA; this will enhance the sensing capacity even more, thus leading to further reduction in the number of receiving elements.

ACKNOWLEDGMENT

This work is funded by NOAA (NA09AANEG0080) and NSF CAREER program (Award # 1653671).

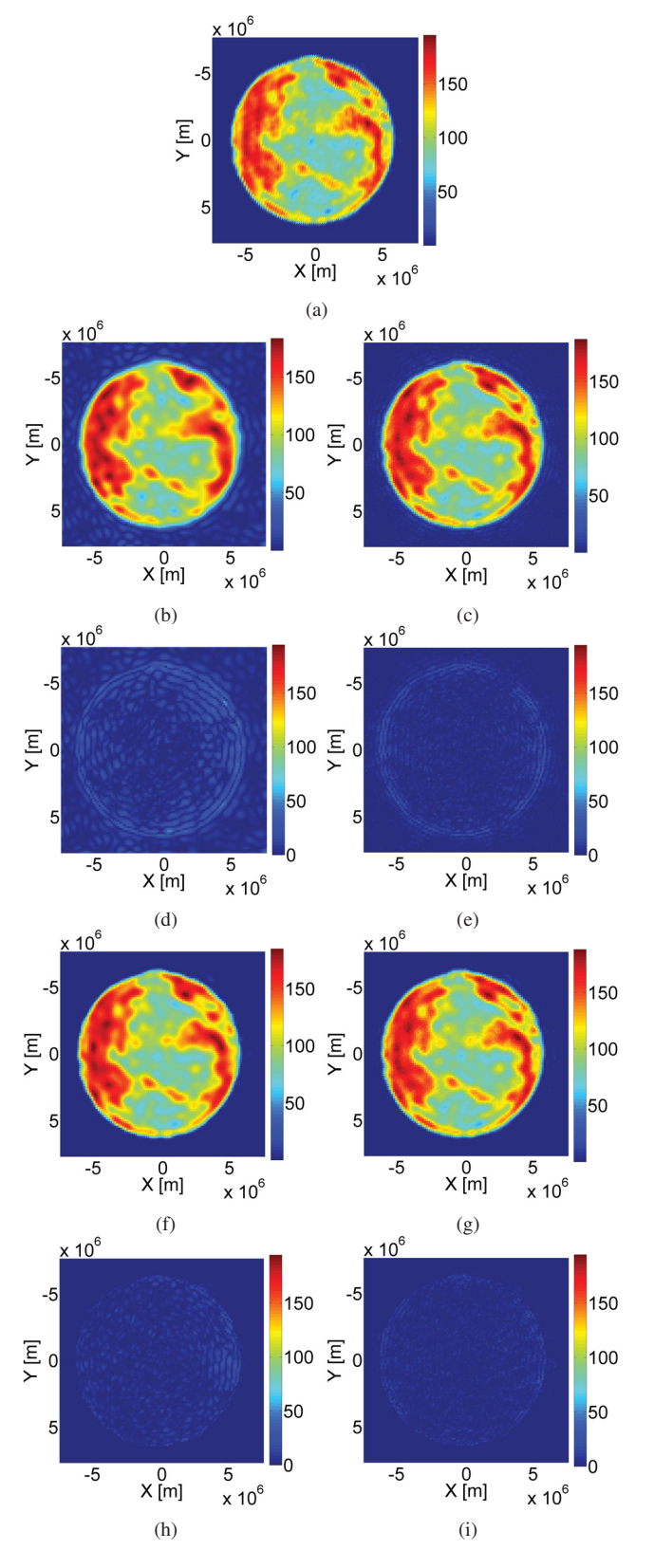


Fig. 13: Image reconstruction for metamaterial-based CRA and GeoSTAR configurations: (a) Original image; reconstruction with pseudo-inverse method for (b) metamaterial-based CRA, and (c) GeoSTAR; error in pseudo-inverse method for (d) metamaterial-based CRA, and (e) GeoSTAR; reconstruction with iterative NESTA method for (f) metamaterial-based CRA, and (g) GeoSTAR; error in NESTA method for (h) metamaterial-based CRA, and (i) GeoSTAR.

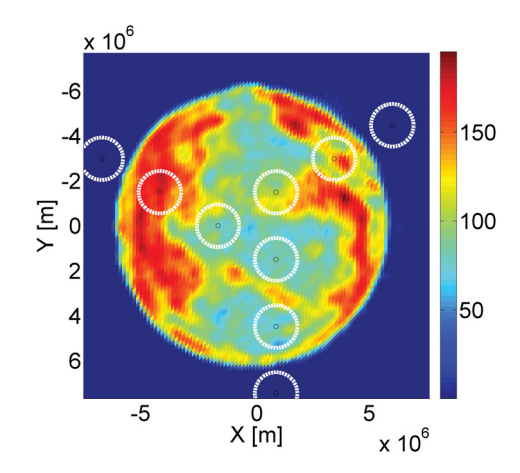


Fig. 14: Half-power beamwidth of the antennas (white circles) covering the surface of the earth when the antennas are exciting the TRA.

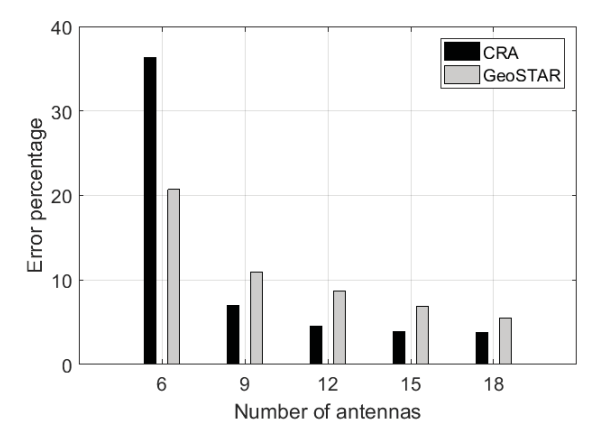


Fig. 15: Error percentage of the GeoSTAR and CRA systems with different number of antenna elements.

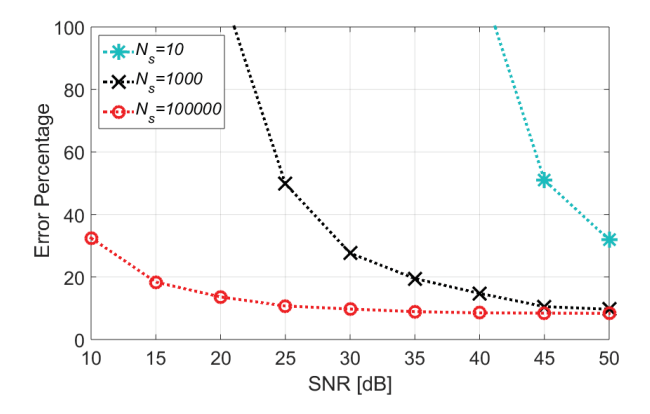


Fig. 16: Reconstruction error of the metamaterial-based CRA as a function of SNR. The measurements are averaged over $N_s=10$, $N_s=1000$, and $N_s=100000$ number of receiving signals.

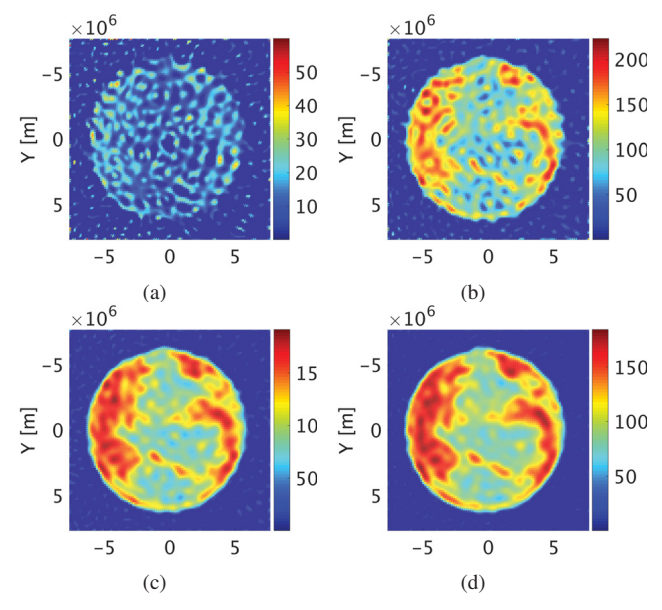


Fig. 17: Reconstructed image for the metamaterial-based CRA configurations with $SNR=50\ dB$. The measurements are averaged over (a) $N_s=1$, (b) $N_s=10$, (c) $N_s=100$, and (d) $N_s=1000$ number of receiving signals.

$\begin{array}{c} \text{Appendix A} \\ \text{Total Reflection Coefficient from a Three-Layer} \\ \text{Medium} \end{array}$

As shown in Fig. 2(a), for any oblique incidence, the EM wave can be decomposed into a TE- and a TM- mode. Using the characteristic impedance of each medium, the transmission and reflection coefficients at each interface can be calculated as described in [40], through the following set of equations:

$$Z_1^{TE} = \frac{\omega(\mu_1 - j\frac{\sigma_{m_1}}{\omega})}{\beta_{\omega}^i - j\alpha_{\omega}^i}; \quad Z_2^{TE} = \frac{\omega(\mu_2 - j\frac{\sigma_{m_2}}{\omega})}{\beta_{\omega}^t - j\alpha_{\omega}^t} \quad (20a)$$

$$Z_1^{TM} = \frac{\beta_{\omega}^i - j\alpha_{\omega}^i}{\omega(\varepsilon_1 - j\frac{\sigma_{e_1}}{\omega})}; \quad Z_2^{TM} = \frac{\beta_{\omega}^t - j\alpha_{\omega}^t}{\omega(\varepsilon_2 - j\frac{\sigma_{e_2}}{\omega})} \quad (20b)$$

$$\Gamma^{TE} = \frac{Z_2^{TE} - Z_1^{TE}}{Z_2^{TE} + Z_1^{TE}}; \quad T^{TE} = \frac{2Z_2^{TE}}{Z_2^{TE} + Z_2^{TE}}$$
 (21a)

$$\Gamma^{TM} = -\frac{Y_2^{TM} - Y_1^{TM}}{Y_2^{TM} + Y_1^{TM}}; \quad T^{TM} = \frac{2}{Y_2^{TM} + Y_1^{TM}}$$
(21b)

where Y_m^{TM} is the admittance of the TM-wave and is given by $Y_m^{TM}=1/Z_m^{TM}.$

The total reflection coefficient Γ from a stratified three-layer medium can be calculated by characterizing the electric and magnetic response of each medium and obtaining the transverse component of the complex wave vector at interfaces of the stratified medium. The generalized stratified structure composing of three lossy isotropic media is depicted in Fig. 2(b). The total reflection Γ is then the superposition of the multiple reflections and transmissions from the two interfaces and is described by the following equation:

$$\Gamma = \Gamma_{12} + T_{12}\Gamma_{23}T_{21}e^{-j2\Phi^{trans}} + T_{12}\Gamma_{23}^2\Gamma_{21}T_{21}e^{-j4\Phi^{trans}} + \dots$$

$$= \Gamma_{12} + T_{12}\Gamma_{23}T_{21}e^{-j2\Phi^{trans}} \cdot \sum_{n=0}^{\infty} q^n$$
(22)

in which the infinite summation is obtained as follows:

$$\sum_{n=0}^{\infty} q^n = \frac{1}{1-q}; \qquad q = \Gamma_{23} \Gamma_{21} e^{-j2\Phi^{trans}}$$
 (23)

In equation (22), Γ is the total reflection coefficient of the structure. Γ_{ij} and T_{ij} are, respectively, the reflection and transmission coefficients associated with the interface between medium i and medium j. The term $e^{-j\Phi^{trans}}$ accounts for the phase delay and amplitude attenuation associated with the wave traveling from the first interface into the second one, or vice versa, and it is computed as $e^{-j\Phi^{trans}} = e^{-jk_2^t \cdot r} = e^{-j\beta_2^t \cdot r} e^{-\alpha_2^t \cdot r}$, with r being the distance vector defined as $r = d_u \hat{u} + d_w \hat{w}$, where

$$d_{u} = \frac{\beta_{2u}^{t}}{\beta_{2w}^{t}} d_{w}; \ d'_{u} = \frac{\alpha_{2u}^{t}}{\alpha_{2w}^{t}} d_{w}; \tag{24}$$

Therefore, the Φ^{trans} term can be written as:

$$\Phi^{trans} = (\beta_{2w}^t d_w + \beta_{2u}^t d_u) - j(\alpha_{2w}^t d_w + \alpha_{2u}^t d_u')
= (\beta_{2w}^t + \frac{\beta_{2u}^{t^2}}{\beta_{2w}^t}) d_w - j(\alpha_{2w}^t + \frac{\alpha_{2u}^{t^2}}{\alpha_{2w}^t}) d_w$$
(25)

Having simplified the infinite summation in equation (23) and calculated the Φ^{trans} term, equation (22) can be reduced as follows:

(20a)
$$\Gamma = \Gamma_{12} + \frac{T_{12}\Gamma_{23}T_{21}e^{-j2\Phi^{trans}}}{1 - \Gamma_{23}\Gamma_{21}e^{-2j\Phi^{trans}}}$$
(20b)
$$= \frac{\Gamma_{12} - \Gamma_{12}\Gamma_{23}\Gamma_{21}e^{-j2\Phi^{trans}} + T_{12}\Gamma_{23}T_{21}e^{-j2\Phi^{trans}}}{1 - \Gamma_{23}\Gamma_{21}e^{-2j\Phi^{trans}}}$$
(26)

REFERENCES

- [1] A. B. Tanner, W. J. Wilson, B. H. Lambrigsten, S. J. Dinardo, S. T. Brown, P. P. Kangaslahti, T. C. Gaier, C. S. Ruf, S. M. Gross, B. H. Lim et al., "Initial results of the geostationary synthetic thinned array radiometer (geostar) demonstrator instrument," *IEEE Trans. Geosci. Remote Sens.*, vol. 45, no. 7, pp. 1947–1957, 2007.
- [2] B. Lambrigtsen, A. Tanner, T. Gaier, P. Kangaslahti, and S. Brown, "Prototyping geostar for the path mission," in *Proc. NASA Sci. Technol. Conf.*, 2007, pp. 19–21.
- [3] B. Picard and E. Anterrieu, "Comparison of regularized inversion methods in synthetic aperture imaging radiometry," *IEEE trans. geosci.* remote sens., vol. 43, no. 2, pp. 218–224, 2005.
- [4] E. L. Kpré and C. Decroze, "Passive coding technique applied to synthetic aperture interferometric radiometer," *IEEE Geosci. Remote Sens. Lett.*, 2017.
- [5] B. Lambrigtsen, W. Wilson, A. Tanner, T. Gaier, C. Ruf, and J. Piep-meier, "Geostar-a microwave sounder for geostationary satellites," in *IEEE Proc. IGARSS'04*, vol. 2, 2004, pp. 777–780.
- [6] H. Lee, J. Park, and H. Lee, "Design of double negative metamaterial absorber cells using electromagnetic-field coupled resonators," in *IEEE Proc. APMC*, 2011, pp. 1062–1065.

- [7] C. M. Watts, X. Liu, and W. J. Padilla, "Metamaterial electromagnetic wave absorbers," *Advanced materials*, vol. 24, no. 23, pp. OP98–OP120, 2012.
- [8] N. Landy, S. Sajuyigbe, J. Mock, D. Smith, and W. Padilla, "Perfect metamaterial absorber," *Phys. rev. lett.*, vol. 100, no. 20, p. 207402, 2008.
- [9] H. Li, L. H. Yuan, B. Zhou, X. P. Shen, Q. Cheng, and T. J. Cui, "Ultrathin multiband gigahertz metamaterial absorbers," *J. of Appl. Phys.*, vol. 110, no. 1, p. 014909, 2011.
- [10] S. Bhattacharyya and K. V. Srivastava, "Ultra thin metamaterial absorbers using electric field driven lc (elc) resonator structure," in *Progress In Electromagnetics Res. Symp.*, 2012, pp. 27–30.
- [11] O. Yurduseven, M. F. Imani, H. Odabasi, J. Gollub, G. Lipworth, A. Rose, and D. R. Smith, "Resolution of the frequency diverse metamaterial aperture imager," *Progress In Electromagnetics Res.*, vol. 150, pp. 97–107, 2015.
- [12] J. Hunt, T. Driscoll, A. Mrozack, G. Lipworth, M. Reynolds, D. Brady, and D. R. Smith, "Metamaterial apertures for computational imaging," *Science*, vol. 339, no. 6117, pp. 310–313, 2013.
- [13] R. Obermeier and J. A. Martinez-Lorenzo, "Model-based optimization of compressive antennas for high-sensing-capacity applications," *IEEE Antennas Wireless Propag. Lett.*, vol. 16, pp. 1123–1126, 2017.
- [14] A. Molaei, G. Allan, J. Heredia, W. Blackwell, and J. Martinez-Lorenzo, "Interferometric sounding using a compressive reflector antenna," in *IEEE 10th Eur. Conf. Antennas Propag.*, 2016, pp. 1–4.
- [15] J. Martinez Lorenzo, J. Juesas, and W. Blackwell, "Single-transceiver compressive antenna for high-capacity sensing and imaging applications," in 9th Eur. Conf. Antennas Propag., April 2015, pp. 1–3.
- [16] J. H. Juesas, G. Allan, A. Molaei, L. Tirado, W. Blackwell, and J. A. M. Lorenzo, "Consensus-based imaging using admm for a compressive reflector antenna," in *IEEE Int. Symp. Antennas and Propag.* IEEE, 2015, pp. 1304–1305.
- [17] J. Martinez-Lorenzo, J. Heredia Juesas, and W. Blackwell, "A single-transceiver compressive reflector antenna for high-sensing-capacity imaging," *IEEE Antennas Wireless Propag. Lett.*, vol. PP, no. 99, pp. 1–1, 2015.
- [18] A. Molaei, J. H. Juesas, G. Allan, and J. Martinez-Lorenzo, "Active imaging using a metamaterial-based compressive reflector antenna," in *IEEE Int. Symp. Antennas Propag.* IEEE, 2016, pp. 1933–1934.
- [19] J. Meana, J. Á. Martínez-Lorenzo, F. Las-Heras, and C. Rappaport, "Wave scattering by dielectric and lossy materials using the modified equivalent current approximation (meca)," *IEEE Trans. Antennas Propag.*, vol. 58, no. 11, pp. 3757–3761, 2010.
- [20] G. Oliveri and A. Massa, "Bayesian compressive sampling for pattern synthesis with maximally sparse non-uniform linear arrays," *IEEE Trans. Antennas Propag.*, vol. 59, no. 2, pp. 467–481, 2011.
- [21] G. Oliveri, P. Rocca, and A. Massa, "A bayesian-compressive-sampling-based inversion for imaging sparse scatterers," *IEEE Trans. Geosci. Remote Sens.*, vol. 49, no. 10, pp. 3993–4006, 2011.
- [22] M. Carlin, P. Rocca, G. Oliveri, F. Viani, and A. Massa, "Directions-of-arrival estimation through bayesian compressive sensing strategies," *IEEE Trans. Antennas Propag.*, vol. 61, no. 7, pp. 3828–3838, 2013.
- [23] G. Oliveri, P. Rocca, and A. Massa, "Reliable diagnosis of large linear arraysa bayesian compressive sensing approach," *IEEE Trans. Antennas Propag.*, vol. 60, no. 10, pp. 4627–4636, 2012.
- [24] S. Ji, Y. Xue, and L. Carin, "Bayesian compressive sensing," *IEEE Trans. Signal Processing*, vol. 56, no. 6, pp. 2346–2356, 2008.
- [25] A. Beck and M. Teboulle, "A fast iterative shrinkage-thresholding algorithm for linear inverse problems," SIAM J. Imaging Sci., vol. 2, no. 1, pp. 183–202, 2009.
- [26] J. Heredia-Juesas, A. Molaei, L. Tirado, W. Blackwell, and J. Á. Martínez-Lorenzo, "Norm-1 regularized consensus-based admm for imaging with a compressive antenna," *IEEE Antennas Wireless Propag. Lett.*, vol. 16, pp. 2362–2365, 2017.
- [27] S. Boyd, N. Parikh, E. Chu, B. Peleato, and J. Eckstein, "Distributed optimization and statistical learning via the alternating direction method of multipliers," *Found. Trends*® in Mach. Learning, vol. 3, no. 1, pp. 1–122, July 2011.
- [28] S. Becker, J. Bobin, and E. J. Candès, "Nesta: a fast and accurate first-order method for sparse recovery," SIAM J. Imaging Sci., vol. 4, no. 1, pp. 1–39, 2011.
- [29] "Nesta: a fast and accurate first-order method for sparse recovery," Mar. 2011. [Online]. Available: http://www-stat.stanford.edu/~candes/nesta/
- [30] Y. Nesterov, "Smooth minimization of non-smooth functions," *Math. programming*, vol. 103, no. 1, pp. 127–152, 2005.

- [31] —, "A method of solving a convex programming problem with convergence rate o (1/k2)," in *Soviet Math. Doklady*, vol. 27, no. 2, 1983, pp. 372–376.
- [32] V. Y. Fedorov and T. Nakajima, "Negative refraction of inhomogeneous waves in lossy isotropic media," *J. of Optics*, vol. 16, no. 3, p. 035103, 2014.
- [33] G. Lipworth, A. Rose, O. Yurduseven, V. R. Gowda, M. F. Imani, H. Odabasi, P. Trofatter, J. Gollub, and D. R. Smith, "Comprehensive simulation platform for a metamaterial imaging system," *Appl. optics*, vol. 54, no. 31, pp. 9343–9353, 2015.
- [34] I. Ramos-Perez, A. Camps, X. Bosch-Lluis, N. Rodriguez-Alvarez, E. Valencia-Domenech, H. Park, G. Forte, and M. Vall-llosera, "Pausa: A synthetic aperture interferometric radiometer test bed for potential improvements in future missions," *Sensors*, vol. 12, no. 6, pp. 7738–7777, 2012.
- [35] J. W. Goodman, "Statistical optics, a wiley-interscience publication," John Wiley & Sons, Inc, vol. 605, pp. 10158–0012, 2000.
- [36] I. Corbella, N. Duffo, M. Vall-Llossera, A. Camps, and F. Torres, "The visibility function in interferometric aperture synthesis radiometry," *IEEE Trans. Geosci. Remote Sens.*, vol. 42, no. 8, pp. 1677–1682, 2004.
- [37] E. J. Candes, J. K. Romberg, and T. Tao, "Stable signal recovery from incomplete and inaccurate measurements," *Communications on pure and applied mathematics*, vol. 59, no. 8, pp. 1207–1223, 2006.
- [38] A. Massa, P. Rocca, and G. Oliveri, "Compressive sensing in electromagnetics-a review," *IEEE Antennas Propag. Mag.*, vol. 57, no. 1, pp. 224–238, 2015.
- [39] G. Oliveri, N. Anselmi, and A. Massa, "Compressive sensing imaging of non-sparse 2d scatterers by a total-variation approach within the born approximation," *IEEE Trans. Antennas Propag.*, vol. 62, no. 10, pp. 5157–5170, 2014.
- [40] D. H. Staelin, D. H. Staelin, A. W. Morgenthaler, and J. A. Kong, Electromagnetic waves. Pearson Education India, 1994.